Aerospace Science and Technology 120 (2022) 107258

Contents lists available at ScienceDirect

Aerospace Science and Technology

www.elsevier.com/locate/aescte

Computational synthesis of large-scale three-dimensional heterogeneous lattice structures

Zhichao Wang, Ali Y. Tamijani *

Aerospace Engineering Department, Embry-Riddle Aeronautical University, Daytona Beach, FL 32114, United States of America

ARTICLE INFO

Article history:
Received 10 August 2021
Received in revised form 1 November 2021
Accepted 28 November 2021
Available online 1 December 2021
Communicated by Jang-Kyo Kim

Keywords:
Topology optimization
Homogenization
Multi-scale structures
Additive manufacturing
Parallel processing

ABSTRACT

This paper describes a methodology for designing the material distribution and orientation of three-dimensional non-uniform (heterogeneous) lattice structures. Recent advances in additive manufacturing enable fabrication across multiple length scales. Homogenization-based design optimization and the subsequent projection of the optimized design facilitate the synthesis of large-scale microstructures that form lightweight bionic designs. The main aspects of this research are (a) the construction, homogenization-based optimization, and projection of two types of lattices with different degrees of anisotropy and (b) the parallelization of the analysis, optimization, and projection framework in order to handle large-scale meshes and obtain high-resolution, heterogeneous lattice structures. Cubic and octet-truss lattices were selected to demonstrate the ability of the framework to design different types of lattices. A quadcopter arm and an internal wing structure were designed using the optimization and projection framework, verifying its capability to synthesize heterogeneous lattice structures for complex design domains. The ability to change the complexity of optimized microlattices using the characteristic parameters of the lattice is discussed. The relationship between the lattice anisotropy and the optimized, smoothed orientation is investigated, and the optimized design for each lattice is compared with those obtained using conventional design optimization procedures.

1. Introduction

The remarkable properties of lattice structures have been utilized in various applications [1–5]. The response of the lattice structure depends highly on the layout of the lattice. Topology optimization is an efficient method for determining the lattice layout across multiple length scales under given boundary conditions for an objective function and a set of constraints. While early topology optimization methods [6] were based on the homogenized properties of microstructures, later the solid isotropic material with penalization (SIMP) method [7] became more popular. In the SIMP method, the design space is restricted to obtain the solid–void macrostructural layout, which is more feasible for fabrication using conventional manufacturing techniques. Recent advances in additive manufacturing (AM) have enabled the use of homogenization-based topology optimization to design microlattices and enhance the performance of the macrostructure [8–10]. In homogenization-based topology optimization, the effective properties of microlattices for various material distributions are derived using numerical homogenization. The optimization is performed on a coarse mesh, whereas the projection of the homogenized design (de-homogenization [11]) is performed on a fine mesh [12]. This is one of the most appealing features of homogenization-based topology optimization compared with other multiscale optimization methods. For example, while SIMP can be used to design large-scale details [13], more than one billion elements are required in the optimization process of a wing-box structure. In contrast, as will be shown in the current study, homogenization-based topology optimization requires several million elements to perform the optimization procedure, and only the optimized designs are projected on large-scale meshes.

Recently, the SIMP method with the Non-Uniform Rational Basis Spline (NURBS) hyper-surfaces framework has been used to perform topology optimization [14,15]. By using the NURBS hyper-surfaces, a pure geometrical (CAD-compatible) descriptor is utilized to reconstruct the topology. Therefore, the optimized design no longer depends on the quality of the mesh, and this can significantly reduce the computational cost required by the SIMP method. Also, due to the geometrical properties of NURBS hyper-surfaces, various geometric requirements, such as the minimum or maximum length scale [16,17], can be implemented in this framework. Recently, this method has been used to solve optimization

* Corresponding author.
E-mail addresses: wangz6@my.erau.edu (Z. Wang), tamijana@erau.edu (A.Y. Tamijani).

https://doi.org/10.1016/j.ast.2021.107258
1270-9638/

Nomenclature

A	Cell domain
$\mathbf{C}$	Stiffness tensor of the lattice material
$\mathbf{C}^H(\mathbf{h})$	Homogenized stiffness tensor
$\mathbf{e}(\mathbf{u})$	Strains
$\mathcal{F}$	Compliance objective function
$\mathbf{f}$	External load vector
$\mathbf{g}$	Reciprocal lattice vector
(h_1, h_2, h_3)	Lattice parameterizations
$\mathbf{n}_i$	Corresponding orthonormal bases of the orientation $(\theta_1, \theta_2, \theta_3)$
$\mathbf{p}$	Linear combination of primitive vectors
$P_\theta(\boldsymbol{\theta})$	Penalty function
$\mathbf{Q}(\boldsymbol{\theta})$	Rotation matrix
$\mathbf{R}(\boldsymbol{\theta})$	Transformation matrix
$\mathbf{r}$	Position vector
$\mathbf{u}$	Displacement vector
V	Volume of the design domain
V_f^{max}	Allowed volume fraction
ψ_n	Binary lattice for the n^{th} distance function
b^n_{pqk}	Amplitude of the pqk^{th} harmonic
$\boldsymbol{\varepsilon}^{(0)kl}$	Macroscopic unit strain
$\boldsymbol{\chi}^{kl}$	Displacement fields
v_i	Virtual displacement field
$\rho(\mathbf{h})$	Density function
$(\theta_1, \theta_2, \theta_3)$	Three Euler angles
γ_c	Weights assigned to the compliance
γ_θ	Weights assigned to the penalty function
Ω_e	Volume of each element
$\max(l_e)$	Maximum length of the edge of the elements
Φ_{pqk}	Mapping function
γ_i	Local dilation

problems that involved requirements concerning structural displacements [18], eigen-frequencies [19], and local stresses [20], and the method also has been used to solve multi-scale topology optimization problems [21].

The two-dimensional (2D) de-homogenization process first was introduced by Pantz and Trabelsi [22] for rank-two laminates. Later, the process was enhanced by Groen and Sigmund [23] and by Allaire, Geoffroy-Donders, & Pantz [24] for a square cell with a rectangular hole. The 2D de-homogenization process was extended to three-dimensional (3D) applications by Geoffroy-Donders, Allaire, and Pantz [25] and Groen et al. [11]. Geoffroy-Donders, Allaire, and Pantz [25] utilized a cubic lattice to perform homogenization-based topology optimization, with a variational formulation constructed in each iteration to regularize the whole orientation matrix instead of individual orientation angles. Groen et al. [11] used a rank-three laminate to perform the optimization, and they implemented a penalty function in the optimization objective to control the changes in orientation in neighboring elements.

Homogenization-based approaches have shown promise in the optimization of microlattices in order to enhance the performances of macrostructures, but to date, they have not been applied in complex applications. The main reason is that, while homogenization-based optimization is performed on a moderate size mesh, it is still computationally expensive when applied to a complex design geometry. Previously, parallel computing has been utilized for topology optimization [26–35] to address computational efficiency, but to the best of the authors' knowledge, it has not been used for homogenization-based optimization and the de-homogenization process. The primary goal of this study is to develop a framework for the homogenization-based optimization and subsequent de-homogenization of large-scale, 3D lattice structures. To this end, we implemented a parallel analysis method and a parallel optimization algorithm. The optimization and de-homogenization framework was developed using FreeFem++, a high-level, finite element programming language written in C++ [36]. An overlapping domain decomposition method, which already has been implemented in FreeFem++, was utilized to solve the Helmholtz-type filtering [37] and elasticity equations. The method of moving asymptotes (MMA) [38] was used for the homogenization-based optimization. While MMA is not available in FreeFem++, a PETSc-based parallel version of MMA has been created by Aage et al. [39]. This parallelized MMA is linked to FreeFem++ via a C++ header file. Note that the parallelized MMA is based on the non-overlapping domain decomposition method. Therefore, a set of macros based on the FreeFem++ integrated message passing interface (MPI) functions was created to re-assemble the global array and create a non-overlapping input for MMA.

To maximize the stiffness of the macrostructure under a volume constraint, the projected optimized lattices have various sizes, material distributions, and orientations. Lattices with spatially varying strut thicknesses are called heterogeneous periodic lattice structures [40]. The second goal of this research was to utilize two types of lattices to synthesize lattice structures. This was accomplished by representing the periodic lattice using spatial harmonics. As we have shown for 2D cases [41,42], the decomposition of the spatial harmonics can be adapted to different types of cells and lattices, thus allowing any types of lattices to be implemented in the optimization and de-homogenization process. The relationships between the orthotropic properties of the lattice and the optimized structural layout, lattice orientation, and structural performance are studied.

The third goal of this research was to investigate the complexity of the optimized layout. Although the proposed framework is capable of designing large-scale details, a designer may choose to reduce the complexity and observe the evolution of the optimized lattice design toward conventional, optimized designs. Thus, the relationship between the complexity of the optimized microlattices and the constraints on the parameters used to represent the lattice geometry was investigated.

Finally, the use of the proposed framework in aerospace applications is discussed. A quadcopter arm and internal wing structures were designed using a cubic lattice and an octet-truss lattice. The optimized lattice designs are compared with those obtained using conventional optimization methods. The complexity of the optimized lattice structures and the improvement in stiffness compared with other designs are presented, and the application of each lattice is discussed.

This article is organized as follows: In Section 2, the parameterization and construction of the selected lattices are discussed. In Section 3, the homogenization-based topology optimization framework and the optimized homogenized results for a test case are presented. The de-homogenization procedure to project the lattices from optimized homogenized results and the comparison between the homogenized and projected designs are discussed in Section 4. In Section 5, the use of the current framework to design an internal wing-box is discussed. The conclusions based on the current framework are discussed in Section 6.

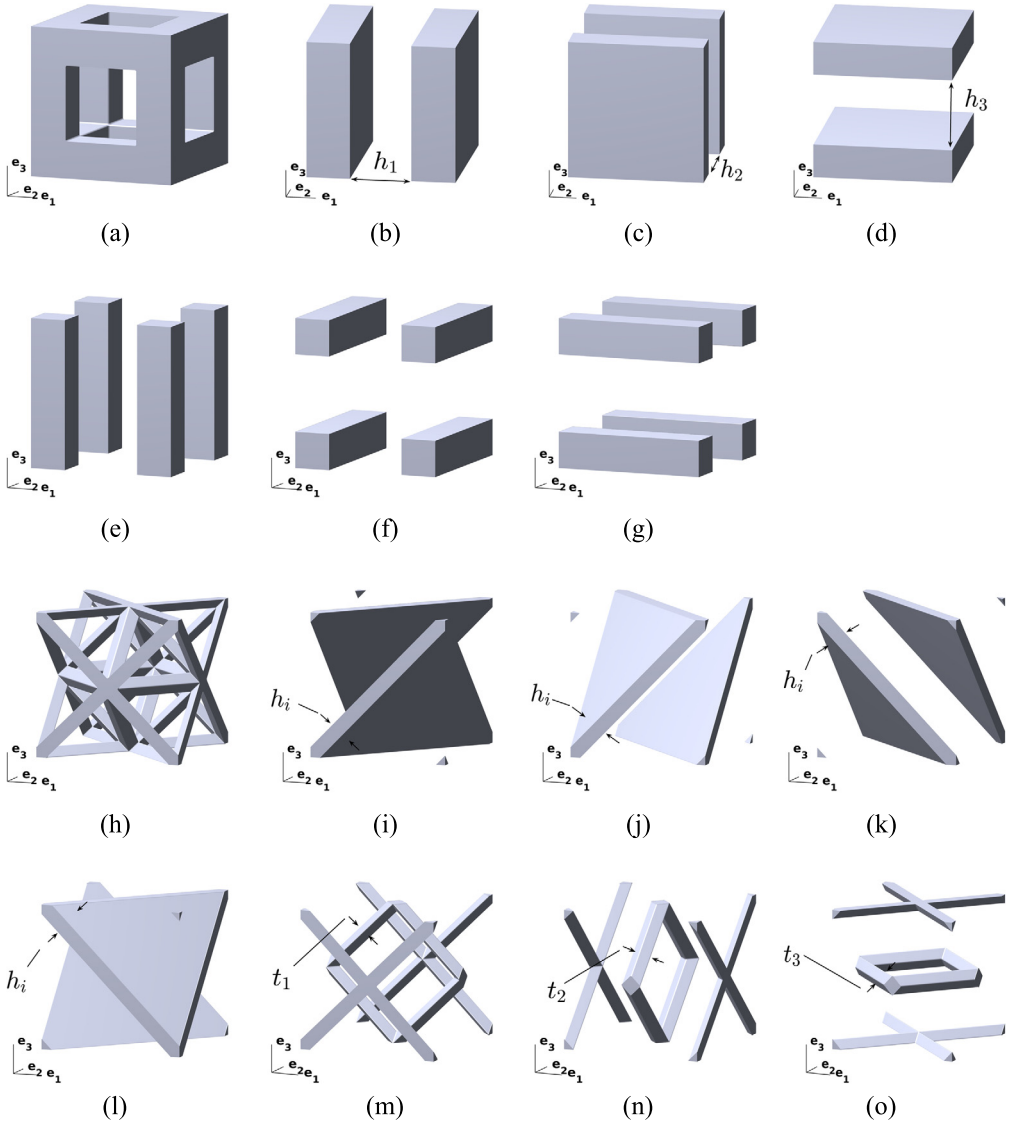

Fig. 1. Construction of a unit cell: (a) Cubic lattice and the corresponding walls to generate distance functions: (b) ψ_1, (c) ψ_2, (d) ψ_3, and the intersection of truncated distance functions: (e) $\psi_1 \cap \psi_2$; (f) $\psi_1 \cap \psi_3$; (g) $\psi_2 \cap \psi_3$. (h) Octet-truss lattice and the corresponding walls to generate distance functions: (i) ψ_1, (j) ψ_2, (k) ψ_3, (l) ψ_4, and combinations of intersection and union of various truncated distance functions: (m) $(\psi_1 \cap \psi_2) \cup (\psi_3 \cap \psi_4)$, (n) $(\psi_3 \cap \psi_1) \cup (\psi_2 \cap \psi_4)$, (o) $(\psi_1 \cap \psi_4) \cup (\psi_2 \cap \psi_3)$.

2. Three-dimensional periodic cellular microstructures

The first step in the process of optimizing the 3D cellular structure is choosing the type of lattice. In this research, two types of lattices from the cubic group were selected, i.e., a cubic lattice (Fig. 1(a)) and an octet-truss lattice (Fig. 1(h)). The former is a simple cubic lattice, and the latter is a face-centered-cubic lattice. Cubic lattices often have been used in compliance-based homogenized topology optimization under a single load case due to their strong orthotropic properties for intermediate densities [25,44]. However, to the best of the authors' knowledge, there is no record of octet-truss lattices being used in homogenization-based optimization, so the current research provides an innovative framework and results for future investigations using this lattice.

Periodic lattices can be described by a linear combination of three primitive vectors as $\mathbf{p} = \mathrm{m}_1\mathbf{a}_1 + \mathrm{m}_2\mathbf{a}_2 + \mathrm{m}_3\mathbf{a}_3$, where m_1, m_2, and m_3 are any integers, and $\mathbf{a}_1$, $\mathbf{a}_2$, and $\mathbf{a}_3$ are three different primitive vectors. The primitive vectors for a cubic lattice and an octet-truss lattice are $(\mathbf{a}_1 = \alpha\mathbf{e}_1, \mathbf{a}_2 = \alpha\mathbf{e}_2, \mathbf{a}_3 = \alpha\mathbf{e}_3)$ and $\left(\mathbf{a}_1 = \frac{\alpha}{2}(\mathbf{e}_1 + \mathbf{e}_2), \mathbf{a}_2 = \frac{\alpha}{2}(\mathbf{e}_2 + \mathbf{e}_3), \mathbf{a}_3 = \frac{\alpha}{2}(\mathbf{e}_1 + \mathbf{e}_3)\right)$, respectively, where $\mathbf{e}_i$ are canonical basis vectors, and α is the cell length.

The second step in the construction of a unit cell is to parameterize the lattice to describe the lattice geometry. Three characteristic parameters were assigned to each unit cell in this research. The three parameters (h_1, h_2, h_3) of the cubic lattice are related to the dimension of the hole along vector $\mathbf{e}_i$ (Fig. 1(b)-(d)). The three parameters of the octet-truss lattice are related to the thickness of the strut along vector $\mathbf{e}_i$, $t_i = \frac{\sqrt{3}}{2}h_i$, where t_i represents the thickness of the strut (Fig. 1(i)-(l)).

After each cell's parameters have been chosen, the next step is to construct the unit cell configuration using a distance function. Then, the distance function is decomposed into spatial harmonics and represented using a Fourier series [41,45], after which the binary lattice can be expressed by:

$$\psi_n = Re\left(\sum_p \sum_q \sum_k b^n_{pqk} e^{\mathrm{j}\mathbf{g}_{pqk}\cdot(\mathbf{r}+\mathbf{p})/\Lambda}\right) \leq h_i, \tag{1}$$

where Re is the real part of the Fourier series, j is the imaginary unit, b^n_{pqk} is the amplitude of the pqk^{th} harmonic, and $\mathbf{r}$ is the position vector. Λ is a scalar to control the periodicity of the lattice, and $\mathbf{g}_{pqk}$ is the reciprocal lattice vector of the pqk^{th} harmonic

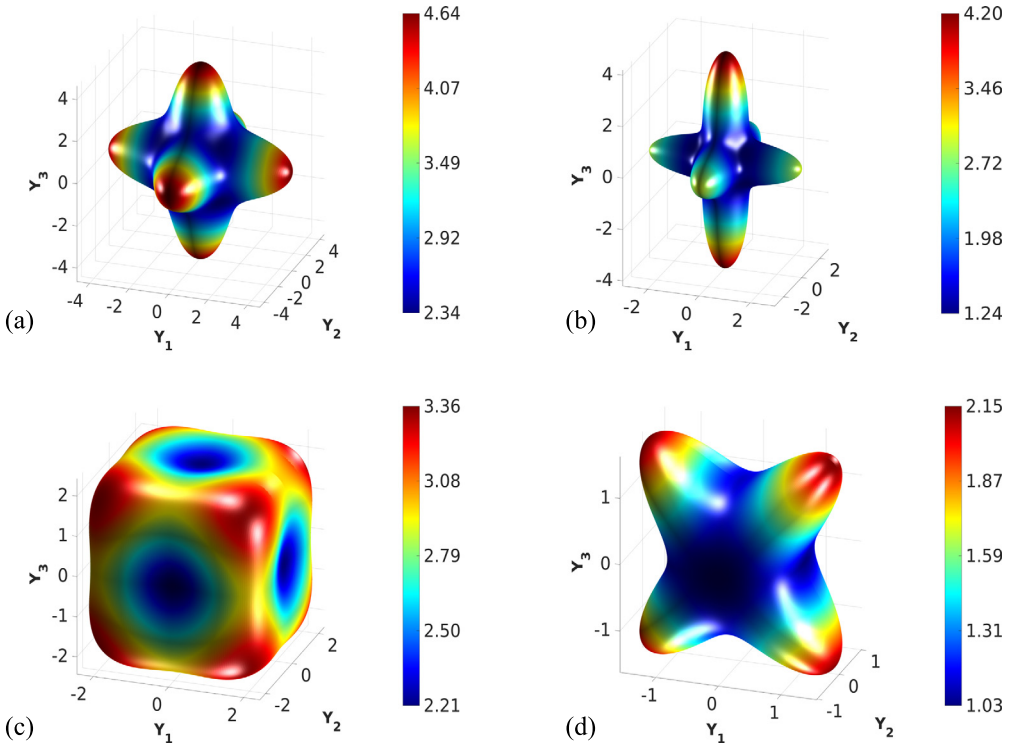

Fig. 2. Effective Young's modulus (GPa) of (a); (b) cubic lattices with $\mathbf{h} = (0.5, 0.5, 0.5)$ and $\mathbf{h} = (0.5, 0.5, 0.7)$; (c), (d) octet-truss lattices with $\mathbf{h} = (0.33, 0.33, 0.33)$ and $\mathbf{h} = (0.33, 0.33, 0.1)$; 25% relative density of (e) cubic lattice with $\mathbf{h} = (0.67, 0.67, 0.67)$ and (f) octet-truss lattice with $\mathbf{h} = (0.174, 0.174, 0.174)$; 40% relative density of (g) cubic lattice with $\mathbf{h} = (0.57, 0.57, 0.57)$ and (h) octet-truss cell with $\mathbf{h} = (0.274, 0.274, 0.274)$; 50% relative density of (i) cubic lattice with $\mathbf{h} = (0.5, 0.5, 0.5)$ and (j) octet-truss lattice with $\mathbf{h} = (0.33, 0.33, 0.33)$. (For interpretation of the colors in the figure(s), the reader is referred to the web version of this article.)

($\mathbf{g}_{pqk} = p\mathbf{g}_1 + q\mathbf{g}_2 + k\mathbf{g}_3$). The reciprocal lattice vector can be written as [43]:

$$\text{Cubic lattice: } \mathbf{g}_1 = \frac{2\pi}{\alpha}\mathbf{e}_1; \quad \mathbf{g}_2 = \frac{2\pi}{\alpha}\mathbf{e}_2; \quad \mathbf{g}_3 = \frac{2\pi}{\alpha}\mathbf{e}_3,$$

Octet – truss lattice:

$$\begin{aligned}
\mathbf{g}_1 &= \frac{4\pi}{\alpha}\left(\frac{1}{2}\mathbf{e}_1 + \frac{1}{2}\mathbf{e}_2 - \frac{1}{2}\mathbf{e}_3\right);\\
\mathbf{g}_2 &= \frac{4\pi}{\alpha}\left(-\frac{1}{2}\mathbf{e}_1 + \frac{1}{2}\mathbf{e}_2 + \frac{1}{2}\mathbf{e}_3\right);\\
\mathbf{g}_3 &= \frac{4\pi}{\boldsymbol{\alpha}}\left(\frac{\mathbf{1}}{\mathbf{2}}\boldsymbol{e_1} - \frac{1}{2}\mathbf{e}_2 + \frac{1}{2}\mathbf{e}_3\right)
\end{aligned} \tag{2}$$

In Eq. (1), b^n_{pqk} is obtained from the Fourier transform of the distance function [45], and ψ_n represents the lattice obtained for the n^{th} distance function. For the cubic lattice, three distance functions are used to generate the three walls of the lattice (ψ_n for $n \in \{1, 2, 3\}$), as shown in Figs. 1(b) - (d). The intersections of the truncated distance functions are generated, as shown in Fig. 1(e)-(g), and the cubic lattice is given by $\psi(\mathbf{h}) = \cup_{1\le i\le j\le 3}\psi_i \cap \psi_j$. This process of generating the cubic lattice geometry was established previously in [25].

For the octet-truss lattice, four distance functions are utilized to generate four wall lattices (ψ_n for $n \in \{1, 2, 3, 4\}$), as shown in Fig. 1(i)-(l). Then, combinations of the intersection and union of various truncated distance functions are implemented to generate three groups of lattices, each corresponding to a thickness, as shown in Fig. 1(m)-(o).

After establishing the geometry of the lattice, the homogenized elasticity tensor is found by applying numerical homogenization [46] over a finite element mesh of cell domain A created by the parameter $\mathbf{h} = (h_1, h_2, h_3)$:

$$\begin{aligned}
&\int_{\mathrm{A}} \mathbf{C}_{ijpq}\left(\frac{\partial \boldsymbol{\chi}^{kl}_p}{dy_q} - \boldsymbol{\varepsilon}^{(0)kl}_{pq}\right)\frac{\partial v_i}{\partial y_j}d\mathrm{A} = 0,\\
&\mathbf{C}^H_{ijkl}(\mathbf{r}) = \frac{1}{|\mathrm{A}|}\int_{\mathrm{A}} \mathbf{C}_{mspq}(\mathbf{r}, \boldsymbol{y})\left(\boldsymbol{\varepsilon}^{(0)kl}_{pq} - \boldsymbol{\varepsilon}_{pq}(\boldsymbol{\chi}^{kl})\right)\\
&\qquad \times \left(\boldsymbol{\varepsilon}^{(0)ij}_{ms} - \boldsymbol{\varepsilon}_{ms}(\boldsymbol{\chi}^{ij})\right)d\mathrm{A}
\end{aligned} \tag{3}$$

where $\boldsymbol{\varepsilon}^{(0)kl}$ are the three macroscopic unit strains, $\boldsymbol{\chi}^{kl}$ are the displacement fields, v_i is the virtual displacement field, and $\mathbf{C}$ is the stiffness tensor of the lattice material. The density function $\rho(\mathbf{h})$ for the cubic lattice is given analytically by $\rho(\mathbf{h}) = (1 - h_1h_2 - h_1h_3 - h_2h_3 + 2h_1h_2h_3)$. To determine the density function for the octet-truss lattice, the summation of the elements' densities over the cell domain is calculated and divided by the volume of the domain, Then, the homogenized properties are calculated for different parameters to build the response surface of $\mathbf{C}^{\mathrm{H}}(\mathbf{h})$. Once the response surfaces have been generated, the sensitivity of the homogenized stiffness tensor $\mathbf{C}^{\mathrm{H}}(\mathbf{h})$ and density $\rho(\mathbf{h})$ with respect to h_i are computed.

To illustrate the orthotropic properties of the two lattices, different sets of parameters (i.e., h_1, h_2, h_3) are selected to plot the effective Young's modulus surfaces in Fig. 2. A point on the surface is given the coordinates $(\mathrm{Y}_1, \mathrm{Y}_2, \mathrm{Y}_3)$. The magnitude of the vector $\mathbf{Y} = \mathrm{Y}_1\mathbf{e}_1 + \mathrm{Y}_2\mathbf{e}_2 + \mathrm{Y}_3\mathbf{e}_3$ formed by the coordinate $(\mathrm{Y}_1, \mathrm{Y}_2, \mathrm{Y}_3)$ and the origin (0,0,0) yields the effective Young's modulus in the direction of vector $\mathbf{Y}$. The material Young's modulus is 15 GPa, and the Poisson's ratio is 0.35. Fig. 2(a) and (b) show the surface plots of the effective Young's modulus with $\mathbf{h} = (0.5, 0.5, 0.5)$ and $\mathbf{h} = (0.5, 0.5, 0.7)$ for the cubic lattice. Fig. 2(a) implies that the cubic lattice with the same thickness of bars gives orthotropic material properties, and the highest Young's modulus (4.64 GPa) occurs in the axial directions $(\mathbf{e}_1, \mathbf{e}_2, \mathbf{e}_3)$. As shown in Fig. 2(b), when the size of the hole in the $\mathbf{e}_3$ direction is increased, the

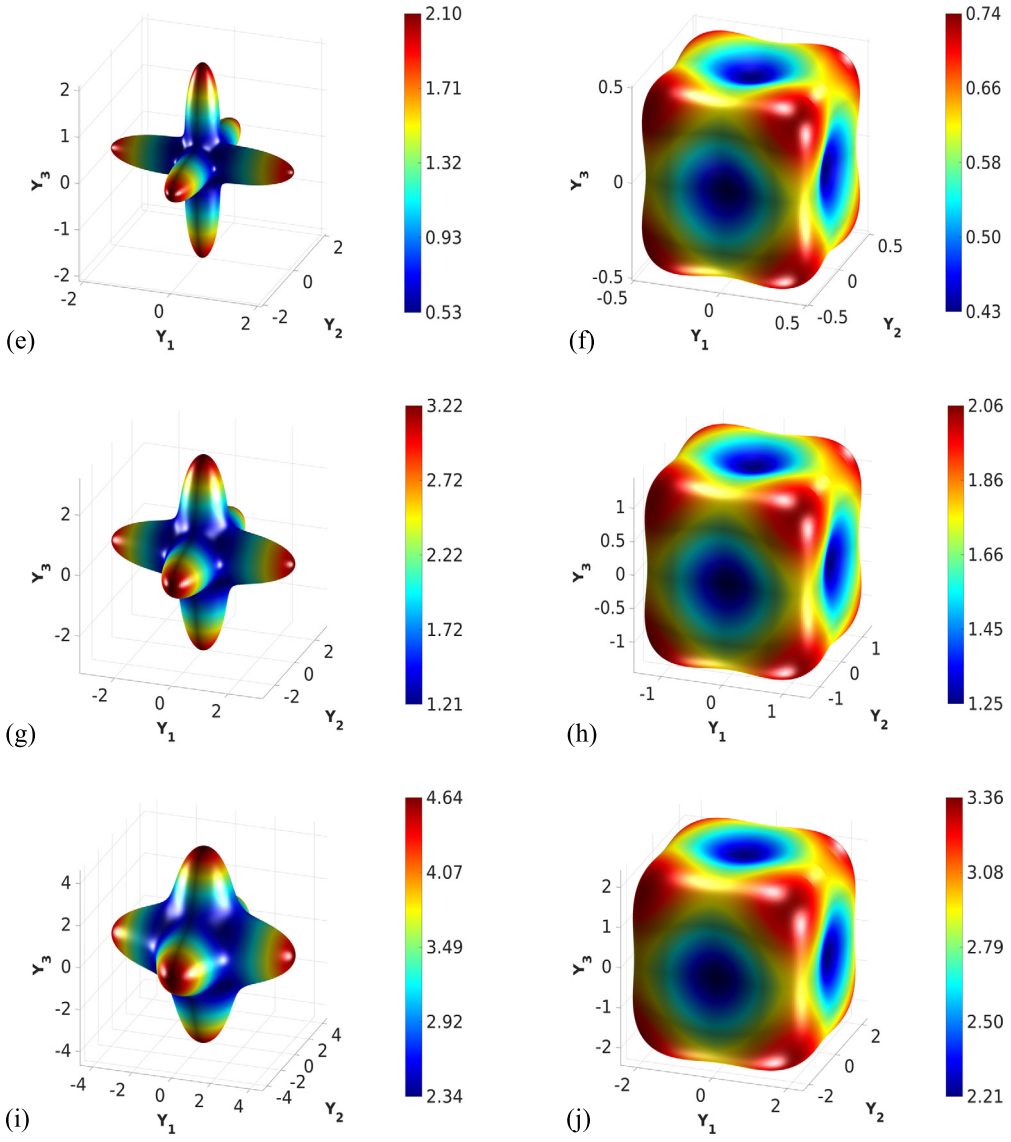

Fig. 2. (*continued*)

thickness of the bars in the $\mathbf{e}_2$ and $\mathbf{e}_1$ (Fig. 1(f) and (g)) directions decreases, and the highest Young's modulus of 4.20 GPa occurs in the $\mathbf{e}_3$ direction.

The effective Young's modulus surface plots with $\mathbf{h} = (0.33, 0.33, 0.33)$ and $\mathbf{h} = (0.33, 0.33, 0.1)$ for the octet-truss lattice are shown in Fig. 2(c) and (d). Fig. 2(c) shows that the octet-truss lattice has orthotropic material properties with equal Young's modulus in the axial directions when all bars have the same thickness. The highest Young's modulus occurs in the diagonal directions, which are not perpendicular, while the lowest Young's modulus occurs in the axial directions. Fig. 2(d) implies that reducing the thickness of the bar in surface $\mathbf{e}_1 \times \mathbf{e}_2$ (the surface formed by vector $\mathbf{e}_1, \mathbf{e}_2$, shown in Fig. 1(o)) shifts the direction of the highest Young's modulus from the diagonal directions to the sub-diagonal directions of surface $\mathbf{e}_1 \times \mathbf{e}_3$.

Fig. 2(e)-(j) show the effective surfaces of the Young's modulus for both lattices with densities of 25%, 40%, and 50%. In general, the cubic lattice has a larger maximum Young's modulus than the octet-truss lattice for the same relative density. The ratios of the maximum Young's modulus in the cubic lattice and the octet-truss cell are 2.83, 1.56, and 1.38 for the 25%, 40%, and 50% relative densities, respectively. Therefore, at a lower relative density, the cubic lattice provides more stiffness than the octet-truss lattice. As the density increases, the advantage of the cubic lattice in terms of the maximum Young's modulus decreases. In addition, Fig. 2 indicates that the effective Young's modulus surfaces of the octet-truss lattice are closer to a sphere for intermediate densities than those of the cubic lattice. This implies that the octet-truss lattice provides weaker orthotropic properties, and the properties are less sensitive to the orientation of the cell than the cubic lattice.

3. Homogenization-based topology optimization

Homogenization-based topology optimization is applied with the aim of minimizing the compliance. This can be formulated as:

$$
\begin{aligned}
&\min_{h_1,h_2,h_3,\theta_1,\theta_2,\theta_3} \mathcal{F}(h_1,h_2,h_3,\theta_1,\theta_2,\theta_3,\mathbf{u}) \\
&s.t.: \mathbf{K}(h_1,h_2,h_3,\theta_1,\theta_2,\theta_3)\,\mathbf{u} = \mathbf{f}, \\
&\quad : \frac{1}{\mathrm{V}} \int_{\Omega} \rho(h_1,h_2,h_3)\, d\Omega - \mathrm{V}_{\mathrm{f}}^{\max} \le 0, \\
&\quad : 0 \le h_1, h_2, h_3 \le 1, \\
&\quad : -4\pi \le \theta_1, \theta_2, \theta_3 \le 4\pi,
\end{aligned}
\tag{4}
$$

where $\mathcal{F}$ is the compliance objective function, V is the volume of the design domain, and V_f^{max} is the allowed volume fraction. Vector $\mathbf{f}$ represents the load applied, $\mathbf{u}$ is the displacement vector, and $\mathbf{K}$ is the global stiffness matrix. The orientations $\boldsymbol{\theta} = (\theta_1, \theta_2, \theta_3)$ are three Euler angles, and the homogenized properties for a different cell orientation are obtained using the transformation matrix, $\mathbf{R}(\boldsymbol{\theta})$:

$$\mathbf{C}_{\boldsymbol{\theta}}(\mathbf{h}, \boldsymbol{\theta}) = \mathbf{R}(\boldsymbol{\theta})^T \boldsymbol{C}(\mathbf{h}) \mathbf{R}(\boldsymbol{\theta}) \tag{5}$$

The transformation matrix, $\mathbf{R}(\boldsymbol{\theta})$, for a symmetric matrix is obtained from a rotation matrix $\mathbf{Q}(\boldsymbol{\theta}) = [\mathbf{n}_1, \mathbf{n}_2, \mathbf{n}_3]$, where $\mathbf{n}_1, \mathbf{n}_2, \mathbf{n}_3$ are the corresponding orthonormal bases of the orientation $\boldsymbol{\theta} = (\theta_1, \theta_2, \theta_3)$. A local penalty function, $P_\theta(\boldsymbol{\theta})$, is added to penalize sudden changes in neighboring elements [11]. Thus, the optimization scheme in Eq. (4) becomes:

$$\begin{aligned}
&\min_{h_1,h_2,h_3,\theta_1,\theta_2,\theta_3} \mathcal{J}(h_1, h_2, h_3, \theta_1, \theta_2, \theta_3, \mathbf{u}) \\
&\quad = \left(\frac{\gamma_c}{\mathcal{F}^0}\right) \mathcal{F}(h_1, h_2, h_3, \theta_1, \theta_2, \theta_3, \mathbf{u}) + \left(\frac{\gamma_\theta}{P_\theta^0}\right) P_\theta(\theta_1, \theta_2, \theta_3) \\
&s.t. : \mathbf{K}(h_1, h_2, h_3, \theta_1, \theta_2, \theta_3)\, \mathbf{u} = \mathbf{f}, \\
&\quad : \frac{1}{V} \int_\Omega \rho(h_1, h_2, h_3)\, d\Omega - V_f^{max} \le 0, \\
&\quad : 0 \le h_1, h_2, h_3 \le 1, \\
&\quad : -4\pi \le \theta_1, \theta_2, \theta_3 \le 4\pi,
\end{aligned} \tag{6}$$

where $\mathcal{F}^0$ and P_θ^0 are the initial compliance and penalty, respectively, and γ_c and γ_θ are the weights assigned to the compliance and penalty functions. Penalty function, $P_\theta(\boldsymbol{\theta})$, is given by:

$$P_\theta = \sum_{f=1}^{n_f} \sum_{i=1}^{3} \left(1 - (\mathbf{n}_i(\boldsymbol{x}_{f,1}) \cdot \mathbf{n}_i(\boldsymbol{x}_{f,2}))^4\right) \tag{7}$$

The penalty function, $P_\theta(\boldsymbol{\theta})$, is looped over all three normal vectors, $\mathbf{n}_1, \mathbf{n}_2, \mathbf{n}_3$, and all of the faces, n_f, that connect the two elements $\mathbf{n}_i(\boldsymbol{x}_{f,1})$ and $\mathbf{n}_i(\boldsymbol{x}_{f,2})$. Equation (7) shows that the highest penalty is applied when the difference between the orientations of neighboring elements is $\frac{\pi}{2}$, and no penalty is applied when the difference between the orientations of neighboring elements is 0 or π. The sensitivity of the objective function and constraint is provided in Appendix A.

The homogenization-based optimization scheme (6) is solved using MMA [38]. The optimization algorithm was developed using FreeFem++ [36]. The state variables, $\mathbf{u}$, are discretized by P_1 finite element functions, and the design variables, including the characteristic parameters $\mathbf{h} = (h_1, h_2, h_3)$ and orientations $\boldsymbol{\theta} = (\theta_1, \theta_2, \theta_3)$, are discretized using P_0 finite element functions. Due to the large-scale design problem, a parallel homogenized-based topology optimization was developed. The available libraries within FreeFem++ for parallelizing the topology optimization include PETSc [47], METIS [48], and MPI. The parallelization in FreeFem++ is based on MPI, and the parallelized algorithm in the current study is organized as follows: (1) The graph partitioner METIS is used to decompose the initial mesh and add several extra layers to obtain a set of overlapping subdomains. (2) Distributed linear systems of PDEs are created, including the 3D elasticity equation and the Helmholtz-type filtering equation for characteristic parameters and related sensitivities. The linear systems are solved using a multigrid preconditioner [49] via PETSc. (3) At each iteration, a parallelized version of MMA [31] is used to update the design variables. The penalty function $P_\theta(\boldsymbol{\theta})$ and its corresponding sensitivity information are constructed based on neighboring information. Thus, the parallelized optimization algorithm is constructed such that the cells on the boundary of a subdomain exchange information with neighboring subdomains. A cantilever beam test case was selected to compare the result of homogenization-based optimization with the results reported by Geoffroy-Donders, Allaire, and Pantz [25]. The discussion is provided in Appendix B.

The arm of a quadcopter is optimized based on the proposed framework. The arm is one of four on the quadcopter (Fig. 3(a)). The dimensions are provided in Fig. 3(b). The displacements in the **x** and **z** directions are fixed for the green surface, and the displacement in the **x** direction is fixed for the red surface. The displacements in the **y** and **z** directions are fixed for the yellow surface, and the displacement in the **y** direction is fixed for the blue surface. There is a hole through which the airscrew is assembled. This hole does not penetrate the entire thickness of the quadcopter; it starts from the top surface and has a unit depth. The material distribution surrounding the hole is fixed as solid, and an upward pressure of 1.68 is applied on the hole surfaces. The volume fraction constraint is 25%. The initial characteristic parameters, h_i, are assigned according to the volume fraction. The initial orientations are set to zero and, after solving the elasticity systems and finding the stresses, the orientations are aligned with the principal stress directions in the first iteration. Then, the characteristic parameters $\mathbf{h} = (h_1, h_2, h_3)$ and orientations $\boldsymbol{\theta} = (\theta_1, \theta_2, \theta_3)$ are updated using MMA in the following iterations. The homogenized properties for both lattices (as obtained in section 2) are utilized in the optimization process.

The quadcopter model is discretized by 1.89 million tetrahedral elements. The optimized design is obtained in five hours using 108 cores of intel Xeon CPU E5-2697 v4 2.3 GHz. In the case of the drone, the suitable weights for the compliance and penalty functions are $\gamma_c = 1$ and $\gamma_\theta = 2$, respectively. The filtering size for homogenization-based topology optimization is $2.5 \times \max(l_e)$, where $\max(l_e)$ is the maximum length of the edge of the elements. For the case study of the quadcopter with 1.89 million elements, $\max(l_e) = 0.15$. In addition, the quadcopter model with 570,000 elements is optimized using the same filtering size (2.5×0.15). Table 1 shows that the optimized compliance is similar for the two meshes. The SIMP design also is obtained for the quadcopter test case. If the homogenization-based filter size is used in SIMP, then some features are omitted, and higher compliance is obtained. Therefore, the SIMP optimization with a smaller filter size of 1.5×0.15 is also considered. The optimized SIMP designs with both filter sizes are shown in Table 1. The optimized SIMP designs with both filter sizes are displayed in Table 1. It is apparent that the cubic lattice optimized design has the lowest compliance, i.e., 1797.21. The SIMP design with the 1.5×0.15 filter size provides lower compliance than the octet-truss lattice design. When the homogenization-based and SIMP optimized results are compared under the same filter size, the homogenized designs achieve significantly better compliance, i.e., 32% and 15% lower for the cubic and octet-truss lattice optimized designs, respectively. These improvements exceeded the 7% reported for the 3D cantilever beam problem in [25].

To visualize the SIMP and homogenization-based optimized designs, the material distribution for each design is transferred to the open-source Paraview application [50]. The SIMP optimized design with the 1.5×0.15 filter size is shown in Fig. 3(c) and (d). The homogenization-based optimized material distributions using the cubic and octet-truss lattices are shown in Fig. 3(e) and (f), respectively. Fig. 4 shows the distributions of the characteristic parameters, **h**, for the cubic and octet-truss lattices.

As shown in Fig. 3(e), the cubic lattice has a higher density close to the surfaces with Dirichlet and Neumann boundary conditions. Intermediate densities appear in the middle of the top and bottom surfaces (as shown in Fig. 3(e)) and inside the design

Table 1
Comparison of final compliance for each test case.

Optimized design	Compliance
Cubic lattice using 1.89 million elements with 2.5×0.15 filtering size	1797.21
Cubic lattice using 540,000 elements with 2.5×0.15 filtering size	1795.58
Octet-truss lattice using 1.89 million elements with 2.5×0.15 filtering size	2125.82
SIMP design using 1.89 million elements with 2.5×0.15 filtering size	2650.57
SIMP design using 1.89 million elements with 1.5×0.15 filtering size	2020.32

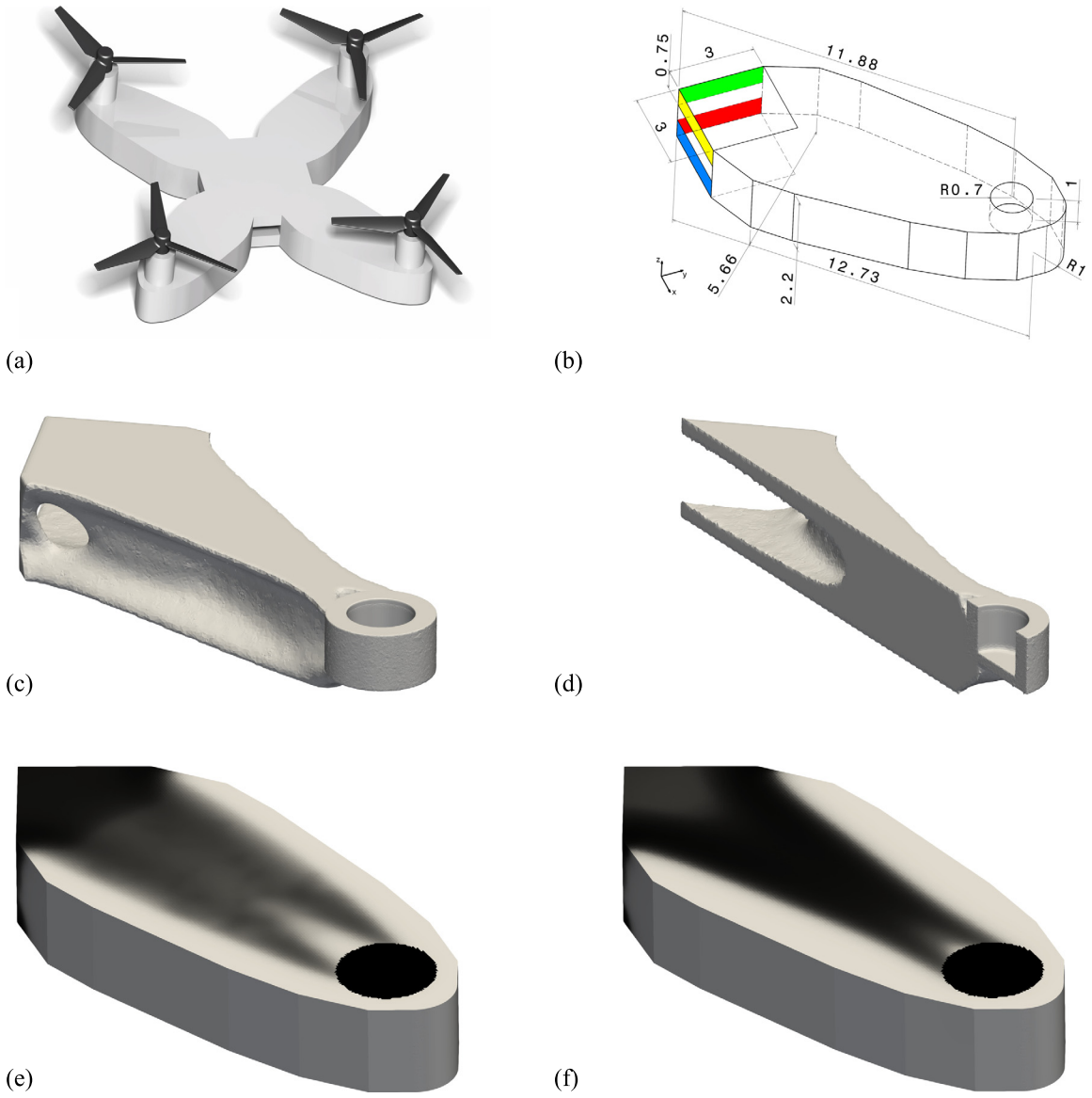

Fig. 3. (a) Entire quadcopter model; (b) dimensions for the quadcopter arm; optimized SIMP material distribution for (c) the quadcopter arm and (d) half of the quadcopter arm; homogenization-based optimized material distribution for (e) the cubic lattice and (f) the octet-truss lattice.

domain. (See Fig. 4(a)-(c).) The large areas with intermediate densities demonstrate the efficient use of the orthotropic properties of cubic lattices. The octet-truss lattice has a narrower density distribution on the top and bottom surfaces (Fig. 3(f)) compared with the cubic lattice. This is because the cubic lattice has a higher effective Young's modulus for the intermediate densities, and it can be oriented toward the perpendicular principal stress directions. This property enables the cubic lattice optimized design to achieve a lower compliance than the octet-truss lattice.

The optimized orientation for the cubic lattice coincides with the principal stress direction. In contrast, the weakest material properties of the octet-truss lattice occur when the cell is oriented toward the principal stress direction. Fig. 5(a) and (b) show the convergence history of compliance for 25% and 50% volume fractions for both lattices. As can be seen in Fig. 5(a), the homogenized cubic lattice design experiences a significant reduction in compliance when it is oriented with the principal directions. However, the plot for the octet-truss lattice shows an increase in compliance in the first iteration when the axial directions are aligned with the principal directions, which is its weakest orientation. To address this issue, the orientation optimization for the octet-truss lattice with fixed material distribution can be performed to identify the initial orientation. Fig. 5(a) also shows that the change in compliance for the octet-truss lattice is less than that of the cubic

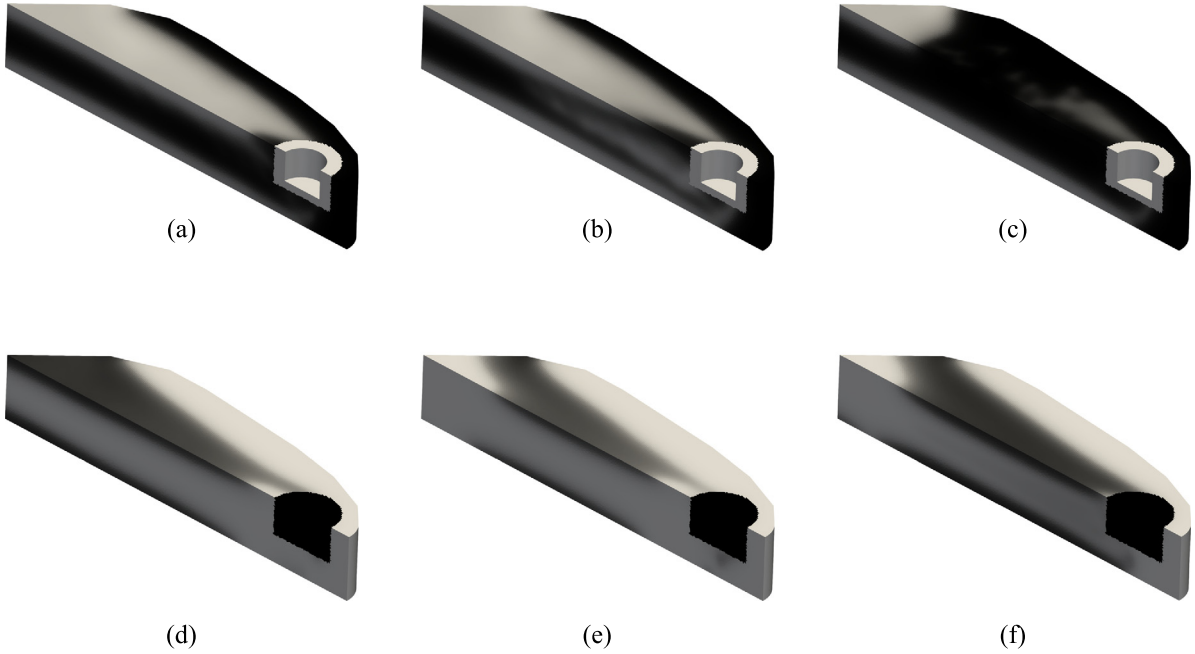

Fig. 4. Optimized characteristic parameter distributions for the half-quadcopter model. (a) h_1, (b) h_2, and (c) h_3 for the cubic lattice design; (d) h_1, (e) h_2, and (f) h_3 for the octet-truss lattice design.

lattice in the first iteration. This is because the octet-truss lattice has a weaker orthotropic property, so it is less sensitive to the cell orientation than the cubic lattice is. After the first iteration, the orientation is optimized based on the sensitivity of compliance, and the octet-truss lattice is oriented away from the principal stress directions.

Next, the changes in compliance for 25% and 50% volume fraction constraints are compared. As can be seen in Fig. 5(a) and (b), when both cells are aligned with the principal directions in the first iteration, the change in compliance for the 25% volume fraction is larger than for the 50% volume fraction. This is because both cells exhibit stronger orthotropic properties at the lower density. This can be seen clearly in Fig. 2, especially for the cubic lattice. In addition, the optimized compliance for the octet-truss lattice with the 50% volume fraction constraint is lower than that for the cubic lattice, unlike the case with the 25% volume fraction constraint. There are two reasons for this, i.e., (1) the difference in the maximum effective Young's modulus between the two lattices is smaller for the higher density and (2) the orientation is regularized during optimization. The penalty function, $P_\theta(\boldsymbol{\theta})$, that is implemented in the optimization scheme (6) results in the regularization of the optimized orientations. Although the stronger orthotropic properties of the cubic lattice are advantageous when the lattice is aligned with the principal stress directions, the smoothed orientations $(\theta_1, \theta_2, \theta_3)$ of the cubic lattice do not necessarily follow the principal directions in the entire design domain, especially for complicated design geometries. Coupled with the smaller difference in effective properties results in the octet-truss lattice exhibiting better performance, as shown in Fig. 5(b).

4. De-homogenization using Fourier series

After obtaining the optimized orientations, the next step is to determine the coherent orientations, $\boldsymbol{\theta}^*$. A π jump is allowed for each direction during the optimization. Although the difference of π does not affect the orientation of the cell, it causes an issue with the construction of the mapping functions to generate continuous lattice structures. Thus, the sign of the direction for each element is evaluated to create a coherent direction in the design domain. Positive signs of n_x, n_y, or n_z were selected as the reference direction, and the direction of each element was changed by π according to the reference direction. Then, the coherent direction, $\mathbf{n}_i^*$, is created. The reciprocal lattice vector is updated as $\mathbf{g}(\boldsymbol{\theta}^*) = \mathbf{Q}(\boldsymbol{\theta}^*)\mathbf{g}$, where $\mathbf{Q}(\boldsymbol{\theta}^*) = [\mathbf{n}_1^*, \mathbf{n}_2^*, \mathbf{n}_3^*]$. Note that the regularization method mentioned above does not address the problem of singularities. For the quadcopter test case, the material in the vicinity of the hole is considered to be solid. Thus, for the test cases studied in this research, no orientation singularities were encountered in the regions with intermediate densities. If a singularity occurs, then the methods suggested in [51,52] can be used.

A mapping function, Φ_{pqk}, is obtained based on the updated reciprocal lattice vector:

$$\begin{aligned} &\nabla^2 \Phi^n_{pqk}(\mathbf{r}) = \nabla . \mathbf{g}^n_{pqk}\left(\boldsymbol{\theta}^*\right)/\Lambda \text{ on } D, \\ &\frac{\partial \Phi^n_{pqk}}{\partial \Gamma} = \mathbf{g}^n_{pqk}\left(\boldsymbol{\theta}^*\right) \cdot \boldsymbol{\eta} \text{ on } \partial\Gamma, \end{aligned} \tag{8}$$

where $\boldsymbol{\eta}$ is the normal vector to the boundary, $\partial\Gamma$. The condition $\nabla\Phi^n_{pqk} \times \mathbf{g}^n_{pqk} = 0$ is applied to ensure that the mapping function is unique. To preserve the original geometry of the cell, local dilation factors [25] are used. A local dilation factor, γ_i, is calculated for each $\mathbf{n}_i^*$, and the new direction $\overline{\mathbf{n}}_i^*$ is calculated as $\overline{\mathbf{n}}_i^* = e^{\gamma_i}\mathbf{n}_i^*$. Then, the new reciprocal lattice vector $\mathbf{g}^n_{pqk}(\overline{\boldsymbol{\theta}}^*)$ is updated as $\mathbf{g}^n_{pqk}(\overline{\boldsymbol{\theta}}^*) = \mathbf{Q}(\overline{\boldsymbol{\theta}}^*)\mathbf{g}^n_{pqk}$, where $\mathbf{Q}(\overline{\boldsymbol{\theta}}^*) = [\overline{\mathbf{n}}_1^*, \overline{\mathbf{n}}_2^*, \overline{\mathbf{n}}_3^*]$. The variational formulation used to calculate γ_i is [25]:

$$\begin{aligned} &\int_D \left(\nabla\gamma_i \wedge \mathbf{n}_i^* + \nabla \wedge \mathbf{n}_i^*\right) \cdot \left(\nabla t \wedge \mathbf{n}_i^*\right) \\ &\quad + \alpha_1^2 \left(\nabla\gamma_i \cdot \mathbf{n}_i^*\right)\left(\nabla t \cdot \mathbf{n}_i^*\right) + \alpha_2^2 \gamma_i t = 0, \end{aligned} \tag{9}$$

where α_1 and α_2 are penalty coefficients. Additional details for the development of Eq. (9) and related penalty coefficients are provided in [25]. For the quadcopter test case, $\alpha_1 = 0.5$ and $\alpha_2 = 0.1$. The next step is to create the binary lattices by using the mapping functions:

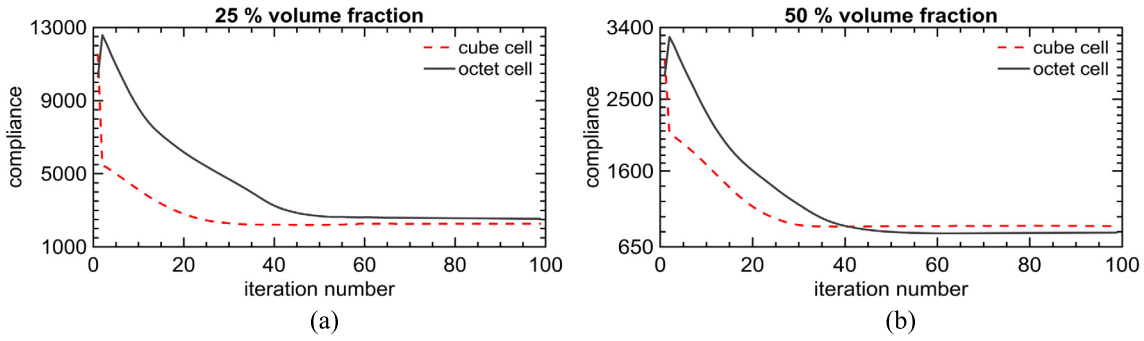

Fig. 5. Convergence history of compliance for the quadcopter model: (a) with 25% volume fractions and (b) with 50% volume fractions.

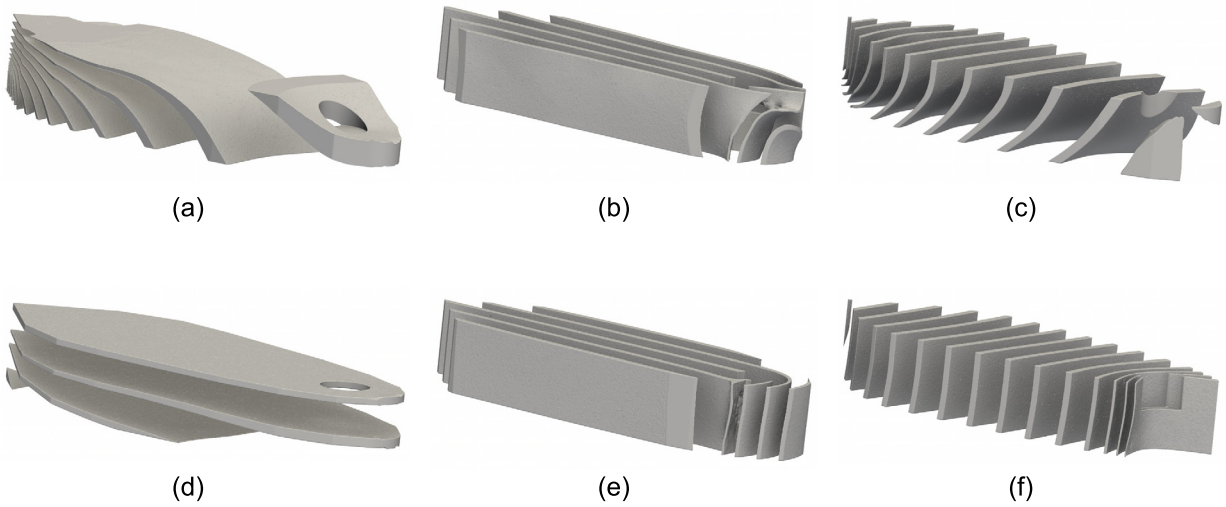

Fig. 6. Regularized directions: (a) $\overline{\mathbf{n}}_1^*$, (b) $\overline{\mathbf{n}}_2^*$, (c) $\overline{\mathbf{n}}_3^*$ for the cubic lattice and (d) $\overline{\mathbf{n}}_1^*$, (e) $\overline{\mathbf{n}}_2^*$, (f) $\overline{\mathbf{n}}_3^*$ for the octet-truss lattice.

$$\psi_n = Re\left\{\sum_{pqk} b^n_{pqk} \exp\left(\mathrm{j}\Phi^n_{pqk}(\mathbf{r})\right)\right\} \leq h_i \tag{10}$$

The parallelized de-homogenization algorithm is implemented in FreeFem++. All the calculations for solving PDEs are applied on the coarse mesh used for the optimization, while the de-homogenization via Fourier series is applied on a fine mesh. The fine mesh for the quadcopter case has approximately one billion elements.

To display the diffeomorphism of each design, the three regularized directions, i.e., $\overline{\mathbf{n}}_1^*, \overline{\mathbf{n}}_2^*, \overline{\mathbf{n}}_3^*$, of the cubic lattice and octet-truss lattice are displayed in Fig. 6(a)-(f). There is a singularity in the region that surrounds the hole. Fortunately, this is not an issue during the projection, as the density is solid near the hole.

To illustrate the morphology of each design, the projected designs with the cubic lattice ($\Lambda = 0.5$) and octet-truss lattice ($\Lambda = 1.0$) with constant parameters $\mathbf{h}$ are plotted in Fig. 7(a) and (c), respectively. The lattice structures with optimized material distributions for the cubic lattice and octet-truss lattice are shown in Fig. 7(b) and (d), respectively.

The displayed lattice structures have rough surfaces, which are inherited from the finite mesh. They also contain disconnected floating members. Therefore, additional post-processing steps are required to create a smooth lattice structure. The first step is to decide the smallest periodicity, t_f, of each cell in Cartesian coordinates. The minimum periodicity of the cubic lattice is equal to Λ. The minimum periodicity of octet solids is $\frac{\sqrt{3}}{8}\Lambda$, as the octet-truss lattice has a thickness of $t_i = \frac{\sqrt{3}}{2}h_i$, and four complete periodicity points exist in one unit cell. Thus, the modified periodicities of the cubic lattice and octet-truss lattice are $\Lambda e^{-\gamma}$ and $\frac{\sqrt{3}}{8}\Lambda e^{-\gamma}$, respectively. The second step of post-treatment is motivated by the process implemented in [24]. In this step, the design domain D is divided into two subsets, i.e. D_1 and D_2. D_1 is the subset of cells with sizes t_f that are less than twice the manufacturable thicknesses h_{min} ($t_f < 2h_{min}$). Voids and solids cannot coexist in subset D_1. The parameter h_i in subset D_1 is modified to obtain $\tilde{h}_i$, where $\tilde{h}_i = 0$ if the cell density $\rho \geq 0.5$ and $\tilde{h}_i = 1$ if the corresponding cell density is less than 0.5, i.e., $\rho < 0.5$. Subset D_2 is the complementary set of D_1 ($t_f \geq 2h_{min}$). The following steps are applied in this subset: (a) $\tilde{h}_i = \frac{h_{min}}{t_f}$ if $\rho > \rho_{th}$ and $t_f h_i < h_{min}$; (b) $\tilde{h}_i = 0$ if $\rho < \rho_{th}$. The final post-processing step is to smooth the surfaces and remove the floating members of the projected solids. These steps were accomplished in MeshLab [53], which is an open-source tool used for mesh processing. Fig. 7(c) and (f) show the projected and post-processed cubic and octet-truss lattices.

5. Lattice structure designs for a generic supersonic fighter wing

The lattice design framework is applied to the more complex test case of a generic supersonic fighter wing. This wing was analyzed previously, and its internal structures were optimized by Locatelli, Mulani, and Kapania [54]. The details of the geometry of the wing are provided in Fig. 8(a) and Table 2. The dimensions of the wing shown in Fig. 8(a) are different from the wing planform reported in [54], because (1) the model was scaled by a factor of 5.2 and (2) a 2.59-mm thickness was attributed to the skin. The thickness of the skin was not shown in [54], and including it in the model resulted in extending the chord by 11.03 mm at the

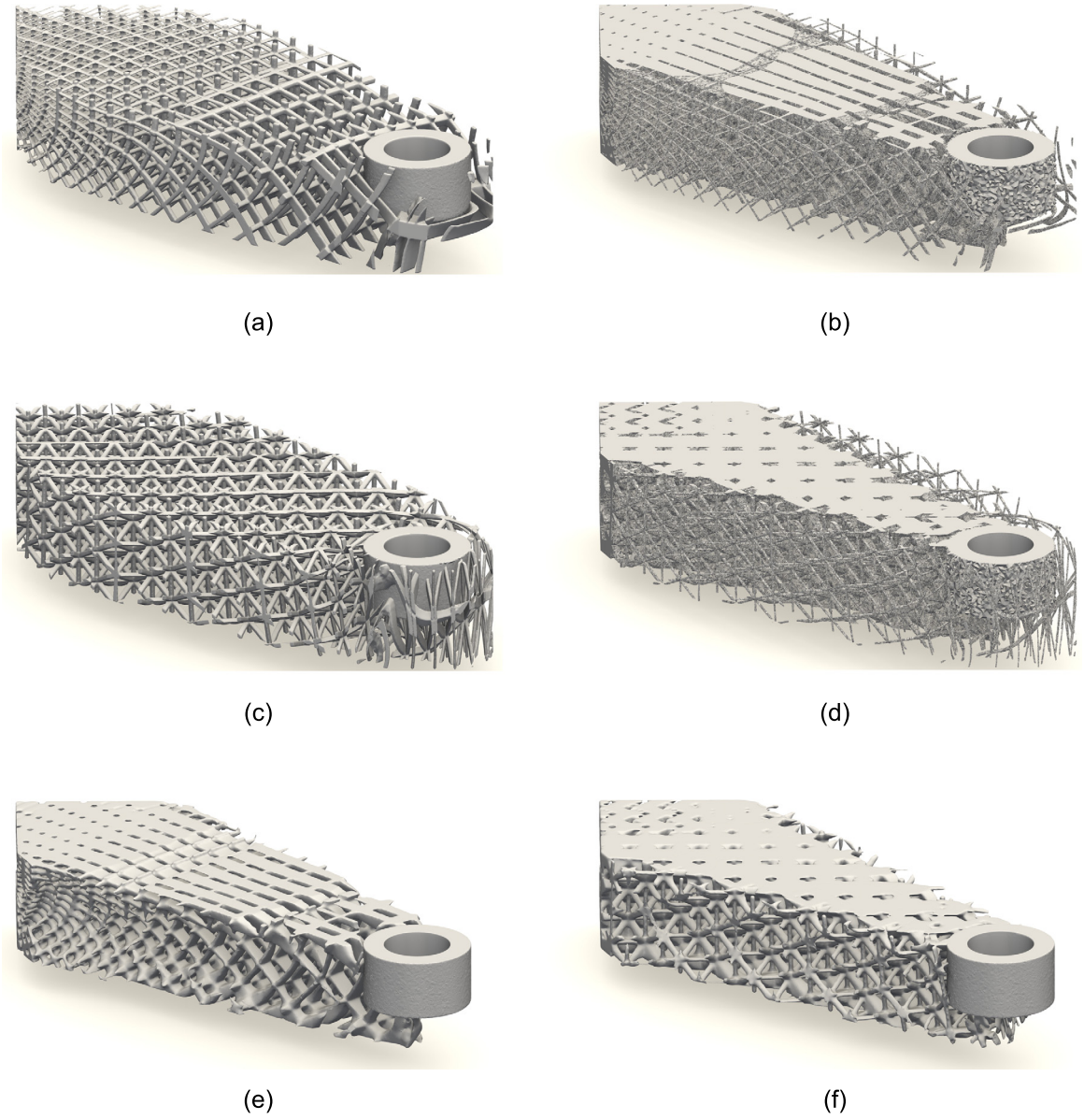

Fig. 7. Projected lattice structures for (a) $\mathbf{h} = (0.8, 0.8, 0.8)$ and (b) optimized material distribution for cubic lattice with $\Lambda = 0.5$; (c) $\mathbf{h} = (0.1, 0.1, 0.1)$ and (d) optimized material distribution for octet-truss lattice with $\Lambda = 1.0$. Post-processed projected lattice structures for (e) cubic lattice and (f) octet-truss lattice.

Table 2
Geometry parameters of the generic supersonic fighter wing.

Dimension	Value
Semi-span (mm)	459.33
Root chord (mm)	535.51
Tip chord (mm)	207.86
Root airfoil thickness (mm)	32.26
Tip airfoil thickness (mm)	12.64
Quarter chord sweep angle (°)	24.03

leading edge and 35.44 mm at the trailing edge so that the top and bottom skins met along a single edge.

The topology and size of the internal structures of the wing-box were designed previously using curvilinear spars and ribs [54], as shown in Fig. 8(b). Although the innovative idea of curvilinear supporting structures enhanced the structural performance (i.e., stiffness, strength, and buckling), the idea stemmed from the traditional design using spars and ribs as supporting structures. Since the fabrication of a wing-box with curvilinear spars and ribs requires an advanced manufacturing technique, such as additive manufacturing, a new lattice-based design paradigm may unlock the full potential of emerging manufacturing techniques. Recently, a computational morphogenesis framework based on SIMP was developed and tested for the design of a wing-box structure [13]. The framework can obtain structural details at various length scales, but it requires more than one billion elements during the optimization process. In addition, while the complexity of the optimized design can be controlled using the size of the filter in the SIMP optimization, the evolution of the optimized design from the spars and ribs-like design to a more complex bionic design is not straightforward. Homogenization-based topology optimization addresses both issues. It requires fewer elements during the optimization process, and only the final design is projected on a fine mesh. As for the complexity, the design domain can be restricted by changing the upper and lower limits of the characteristic parameters to obtain a spars and ribs-like design, with a more complex lattice design emerging as the limits are relaxed. This capability allows the designer to obtain the optimized design in a reasonable computational time and with the desired complexity.

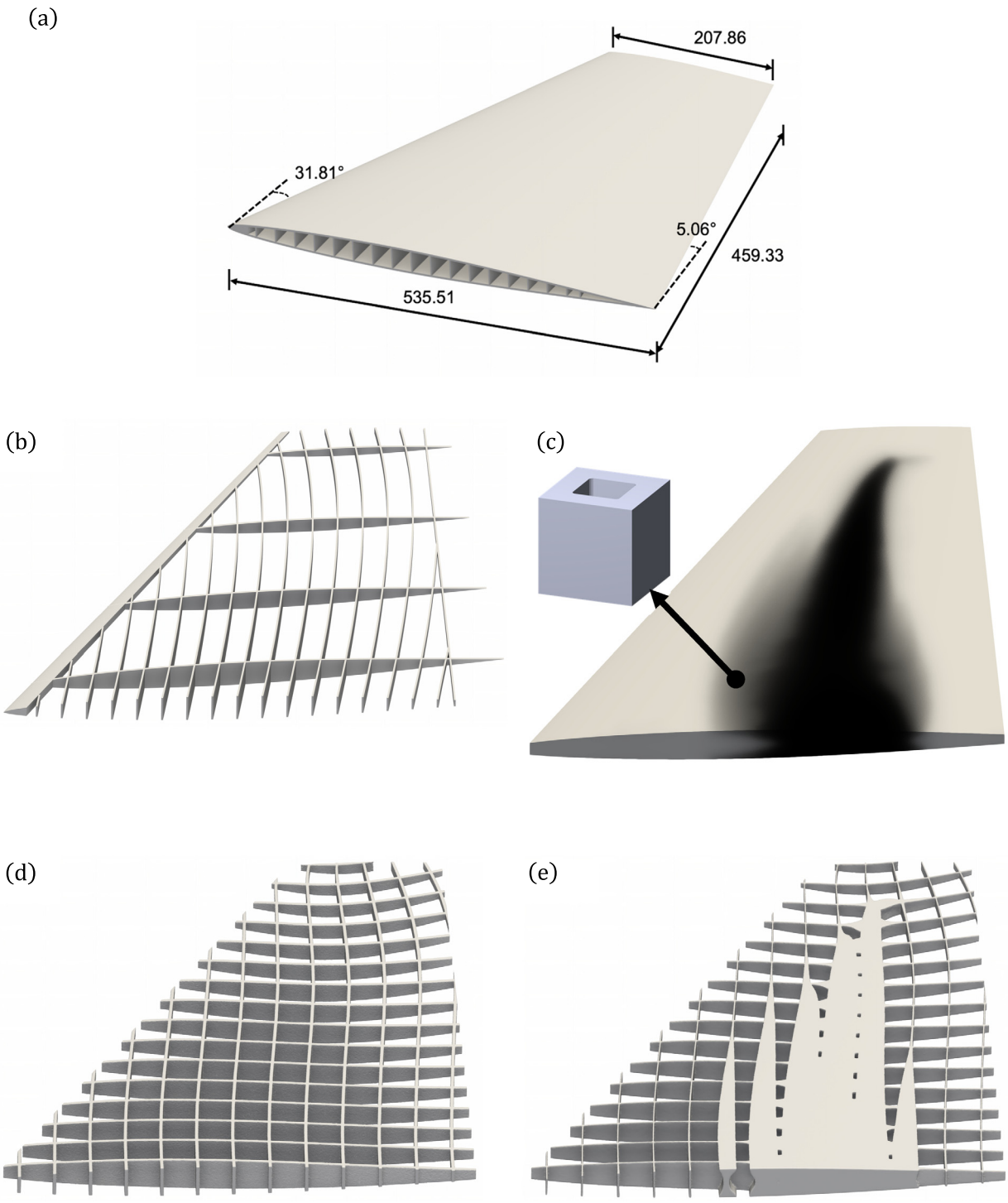

Fig. 8. (a) Generic supersonic fighter wing dimensions (mm); (b) curvilinear design for spars and ribs [54]. Optimized design for cubic lattice for fixed $h_3 = 0.05$: (c) optimized material distribution, (d) projected cubic lattice design with $\mathbf{h} = (0.9, 0.9)$ and $\Lambda = 30$, (e) post-processed projected cubic lattice design.

The wing model is discretized by 3.8 million tetrahedral elements. The wing root is clamped, and an upward uniform pressure of 3.98×10^{-6} N/mm^2 is applied on the top and bottom surfaces. The volume fraction constraint is 40%. To obtain a less complex design with fewer features, the parameter h_3 in the **z** direction (see Fig. 1(a) and (d)) is fixed at 0.05 during the optimization process. This restriction provides continuous surfaces in the **z** direction, similar to the spars and ribs design. For the initial directions, two Euler angles of θ_2 and θ_3 are set to zero and θ_1 is obtained from the principal directions. This restriction on the initial directions ensures that the initial lattices are along the global **z** axis. Then, during the optimization, the three Euler angles are freely rotated in space. The optimized material distributions for the cubic lattices with the abovementioned restrictions are shown in Fig. 8(c). It can be seen that the high density region exists only in the middle of the wing, and the width of this region decreases from the root to the tip of the wing. In addition, the density is higher near the top and bottom surfaces in the **z** direction. The projected optimized cubic lattice design on a 2.5-billion-element fine mesh with constant parameters $\mathbf{h} = (0.9, 0.9, 0.05)$ for $\Lambda = 30$

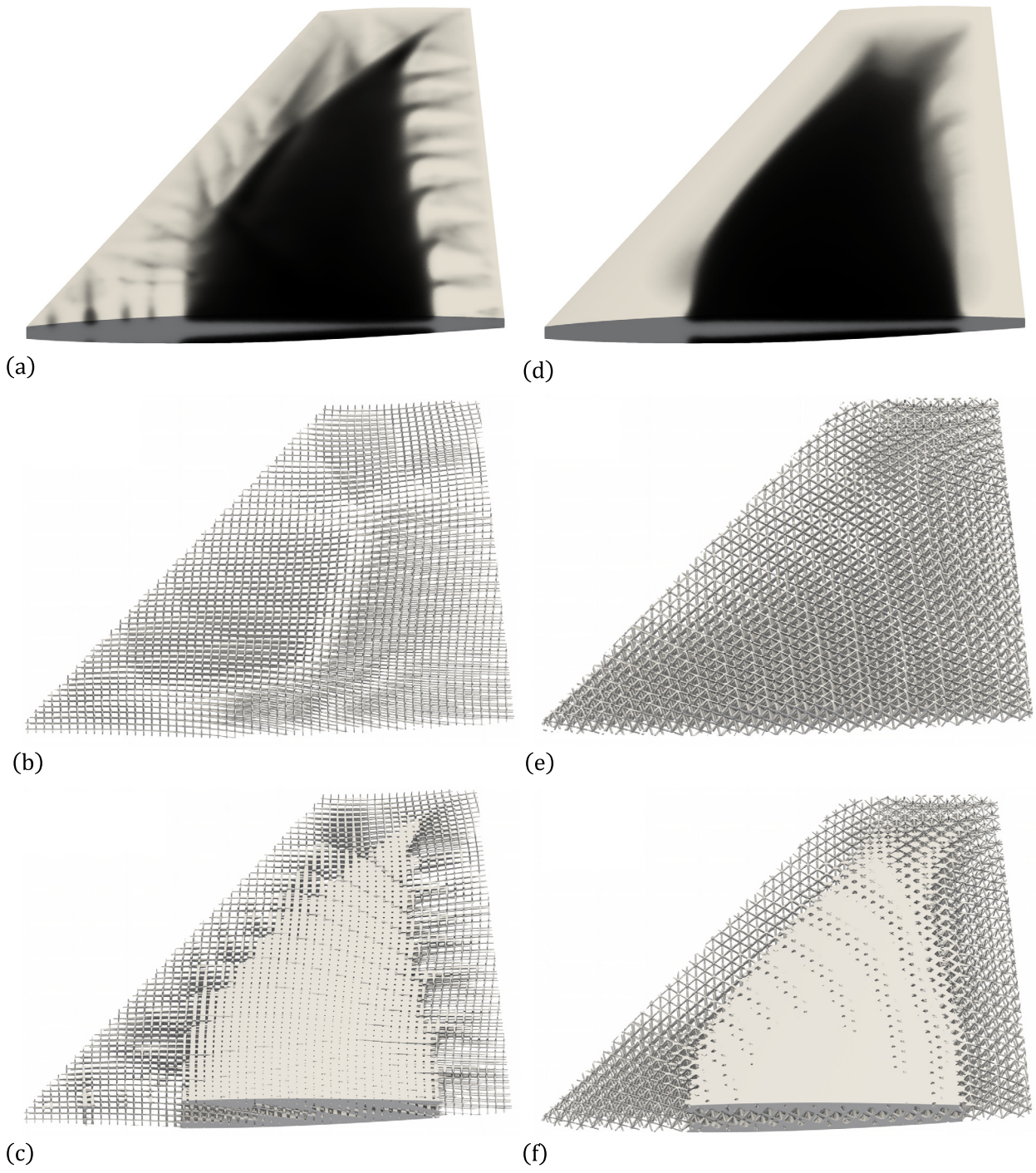

Fig. 9. Optimized lattice design for wing-box structures. Cubic lattice design: (a) optimized material distribution, (b) projected design with $\mathbf{h} = (0.9, 0.9, 0.9)$ and $\Lambda = 7$, (c) post-processed projected design. Octet-truss lattice design: (d) optimized material distribution, (e) projected design with $\mathbf{h} = (0.1, 0.1, 0.1)$ and $\Lambda = 15$, (f) post-processed projected design.

is shown in Fig. 8(d). The constant projected solids have a similar morphology to the curvilinear spars and ribs design [54]. Further, the proposed lattice structure design framework is capable of efficient material utilization with the restricted lattice morphology. The post-processed projected design with the optimized material distribution is shown in Fig. 8(e). It should be noted that, while compliance is minimized subject to a volume constraint in the current study, the minimum weight design under buckling and stress constraints are considered in [54].

Next, the design parameters were relaxed to obtain a more complex design with large-scale details. The optimized material distribution for the cubic lattice is shown in Fig. 9(a). A comparison of the restricted and relaxed cubic lattice designs in Fig. 8(c) and Fig. 9(a) shows that the density is distributed over a larger region in the relaxed design. This is because the cubic lattice with three parameters has greater freedom to distribute material more efficiently. The additional design freedom results in an 8% improvement in compliance compared with the restricted design. (See Table 3.) In terms of orientation, Fig. 9(b) shows that the cubic lattice with three parameters has a more complicated morphology than the restricted cubic lattice design. The post-processed projected cubic lattice design with the optimized density is presented

Table 3
Comparison of compliance in optimized lattice designs for the wing test case.

Optimized design	Compliance
Cubic lattice design with fixed $h_3 = 0.05$	1.41
Cubic lattice design with three characteristic parameters	1.29
Octet-truss lattice design with three characteristic parameters	1.08

in Fig. 9(c). A smaller periodicity ($\Lambda = 7$) compared with the restricted lattice design (Fig. 8(c)) ensures the connectivity of the projected lattices.

Fig. 9(d) shows the optimized distribution of material with the octet-truss lattice. The comparison of the optimized material distributions of the cubic and octet-truss lattices showed that the latter has a smaller intermediate-density area. However, as can be seen in Table 3, the compliance of the optimized octet-truss lattice design is lower than that of the cubic lattice. The same trend was observed for the quadcopter case with the 50% volume fraction constraint. The wing-box design domain is complex, and the smoothed optimized directions deviate from the principal stress directions. When the orientation is regularized during optimization, the lower sensitivity of the octet-truss lattice to the orientation results in 23% and 8% improvement in stiffness compared to the cubic lattice designs.

The projected octet-truss design with the optimized morphology for a constant parameter $\mathbf{h} = (0.1, 0.1, 0.1)$ is illustrated in Fig. 9(e). Fig. 9(f) shows the post-processed projected design with the optimized material distribution.

It should be noted that the wing test case in the current study is an academic benchmark problem. The aerodynamic load, multiple load cases, the fluid-structure interaction, and several important constraints, such as stress, buckling, flutter, and divergence [54–57], are not considered in this study. Another important note is that, while the small features (solids and holes) that are less than certain thresholds as well as the floating members are removed in the post-processed step, other additive manufacturing issues, such as sagging [58] and powder trapping [59], are not addressed here.

6. Conclusion

In this paper, we have described a framework for designing the topology and morphology of large-scale 3D heterogeneous lattice structures. The parallelization of the analysis, optimization, and projection framework provide the capability to design lattice structures for complex design geometries. The use of a Fourier series representation in the construction of the unit cells enables the framework to adapt to various types of lattices. The optimized designs for a quadcopter arm and internal wing structures using cubic and octet-truss lattices were compared. For the quadcopter arm, the cubic lattice provides better stiffness when the optimized directions are close to the principal stress directions and the designed volume fraction is low. Increasing the relative density decreases the difference in the maximum effective Young's modulus between the two lattices. Thus, increasing the volume constraint means that the octet-truss provides greater stiffness. Another important insight is that the regularization of orientations has less effect on the optimized directions for simple design domains because there are fewer irregularities in the optimized orientation. For a complex design domain, such as a wing-box, the regularized orientation is further away from the principal stress direction. The octet-truss lattice has weaker orthotropic properties than the cubic lattice, so it is less sensitive to the orientation of the cell. Thus, the octet-truss lattice provided better stiffness in the wing case study. In addition to implementing various lattices, the framework that was developed allows control of the complexity of the optimized design. The design domain can be restricted by changing the upper and lower limits of the parameters of the lattice characteristic. This may be used, for example, to obtain a spars and ribs-like design for the internal structure of the wing and subsequently relax the limits to obtain a more complex lattice design. Although the quadcopter arm included a hole, it was close to the boundary of the design domain, and the density of the region close to the hole was solid. Thus, there was no effect on the optimized lattice structures. In addition, no singularities were observed in the optimized directions for the test cases studied in this research. However, other test cases may include both non-simply connected domains and singularities [51,52], and so these issues must be considered in the future development of the proposed framework. The aeroelastic analysis and stress and buckling constraints were not considered in the optimization of the internal structure of the wing, and they are subjects for future studies.

Declaration of competing interest

The authors declare that they have no known competing financial interests or personal relationships that could have appeared to influence the work reported in this paper.

Acknowledgements

The authors gratefully acknowledge the support of the National Science Foundation (NSF) under award number 1847133 with program manager, Dr. Kathryn Jablokow.

Appendix A. Sensitivity analysis

The sensitivity of the objective function and constraint is given as Eq. (11)

$$\begin{aligned}
\frac{\partial \mathcal{J}}{\partial h_i} &= -\left(\frac{\gamma_c}{\mathcal{F}_0}\mathbf{e}(\mathbf{u})^T\mathbf{R}(\boldsymbol{\theta})^T\frac{\partial \mathbf{C}(\mathbf{h})}{\partial h_i}\mathbf{R}(\boldsymbol{\theta})\mathbf{e}(\mathbf{u})\right)\Omega_e,\\
\frac{\partial \mathcal{J}}{\partial \theta_i} &= -2\left(\frac{\gamma_c}{\mathcal{F}_0}\mathbf{e}(\mathbf{u})^T\mathbf{R}(\boldsymbol{\theta})^T\mathbf{C}(\mathbf{h})\frac{\partial \mathbf{R}(\boldsymbol{\theta})}{\partial \theta_i}\mathbf{e}(\mathbf{u})\right)\Omega_e\\
&\quad+\left(\frac{\gamma_\theta}{P_0}\left(\sum_{f=1}^{n_f}\sum_{i=1}^{3}(-4\cdot((\mathbf{n}_i(\boldsymbol{\chi}_{f,1})\mathbf{n}_i(\boldsymbol{\chi}_{f,2}))^3)\right.\right.\\
&\quad\left.\left.\cdot\left(\frac{\partial((\mathbf{n}_i(\boldsymbol{\chi}_{f,1})\cdot\mathbf{n}_i(\boldsymbol{\chi}_{f,2}))}{\partial\theta_i}\right)\right)\right),
\end{aligned} \tag{11}$$

where $\mathbf{e}(\mathbf{u})$ is the strains vector, and Ω_e is the volume of each element. The sensitivity of the volume fraction of the cubic lattice can be given analytically as:

$$\begin{aligned}
\frac{\partial}{\partial h_1}\int_\Omega \rho(h_1,h_2,h_3)\,d\Omega &= -(h_2+h_3-2h_2h_3)\,\Omega_e,\\
\frac{\partial}{\partial h_2}\int_\Omega \rho(h_1,h_2,h_3)\,d\Omega &= -(h_1+h_3-2h_1h_3)\,\Omega_e,\\
\frac{\partial}{\partial h_3}\int_\Omega \rho(h_1,h_2,h_3)\,d\Omega &= -(h_1+h_2-2h_1h_2)\,\Omega_e.
\end{aligned} \tag{12}$$

The sensitivity of the volume fraction of the octet lattice is obtained from the response surface $\rho(\mathbf{h})$.

Appendix B. Cantilever beam test case

The cantilever beam test was optimized, and the results were compared with those reported by Geoffroy-Donders, Allaire, and Pantz [25]. The domain size is given as $15 \times 10 \times 5$ and the upper bound of the volume fraction is 35%. A cubic lattice was selected,

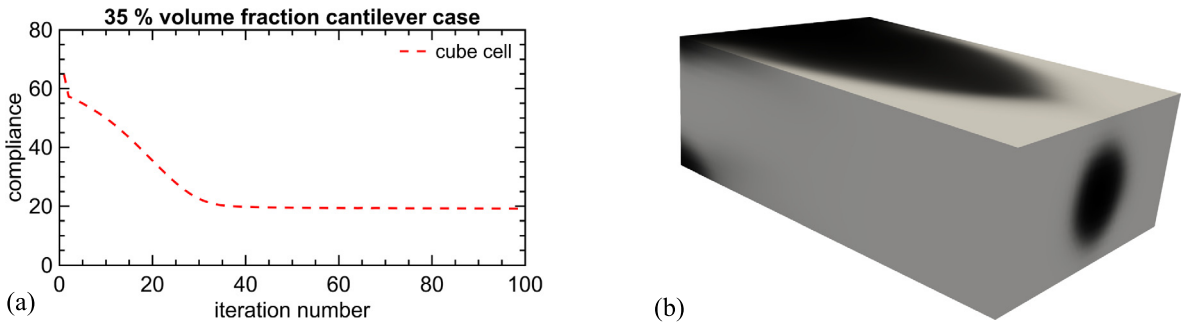

Fig. 10. (a) Convergence history of the compliance; (b) homogenization-based optimized material distribution for the cantilever beam test.

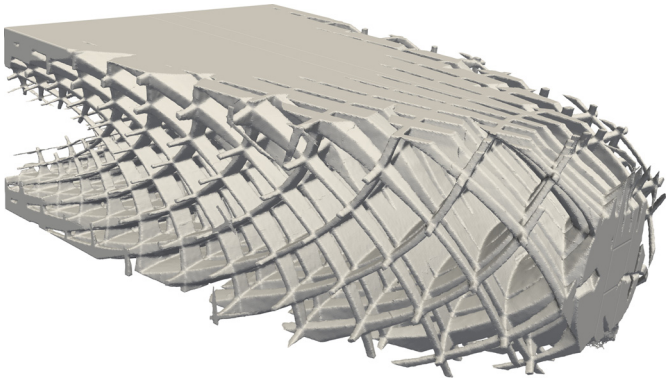

Fig. 11. The projected cubic lattice for cantilever beam test case with $\Lambda = 0.9$.

Table 4
Initial and optimized compliance ($\mathcal{F}^0$ and $\mathcal{F}^*$) and penalty (P_θ^0 and P_θ^*) for various weights (γ_c, γ_θ).

(γ_c, γ_θ)	($\mathcal{F}^0$, $\mathcal{F}^*$)	(P_θ^0, P_θ^*)
($\gamma_c = 1$, $\gamma_\theta = 5$)	(64.81, 22.32)	(48404, 3358)
($\gamma_c = 1$, $\gamma_\theta = 0.5$)	(64.81, 19.24)	(48404, 3996)
($\gamma_c = 1$, $\gamma_\theta = 0.05$)	(64.81, 18.40)	(48404, 5452)

Table 5
Compliance and volume fraction of the projected cubic lattice with various lattice periodicity parameters, Λ.

Periodicity parameter, Λ	Projected volume fraction	Projected compliance
$\Lambda = 1.8$	33.57%	43.7
$\Lambda = 1.35$	33.79%	32.35
$\Lambda = 0.9$	34.11%	23.996
$\Lambda = 0.5$	34.02%	21.01
$\Lambda = 0.2$	34.05%	19.89

and the homogenized properties reported in Section 2 were implemented in the optimization process. Both the type of lattice (cubic lattice) and the properties of the cell material are similar to those utilized in [25]. The design domain was discretized by 39,600 and 3,604 tetrahedral elements in this study and in [25], respectively. In order to investigate the effect of the weights assigned to the compliance and penalty functions (γ_c and γ_θ) on the optimized design, three sets of weights were considered, and the initial and optimized values for compliance and penalty function are reported in Table 4. As can be seen, a large ratio of $\frac{\gamma_c}{\gamma_\theta}$ yields discontinuous orientation vector fields and a large value for P_θ, while a small ratio of $\frac{\gamma_c}{\gamma_\theta}$ makes the algorithm susceptible to finding local minimums for compliance. The suitable ratio of $\frac{\gamma_c}{\gamma_\theta}$ varies for different test cases. It is good practice to obtain the optimized designs for various ratios of $\frac{\gamma_c}{\gamma_\theta}$ using a coarse mesh and determine the appropriate weights. The appropriate weights for this test case were $\gamma_c = 1$ and $\gamma_\theta = 0.5$, which resulted in an optimized compliance of 19.24 and a penalty of 3996. The initial compliance of 64.62 and the optimized compliance of 20.93 were reported in [25], and the results of the current framework were close to those values.

The convergence history of the compliance and the homogenized design of the cantilever beam test case are shown in Fig. 10. Fig. 10(b) shows a more uniform distribution of material compared to the results shown in [25], which could be due to the use of finer mesh in the current study.

The homogenized design is projected by using 9 million tetrahedral elements for various periodicity parameters (Λ). Fig. 11 shows the projected design for periodicity parameters $\Lambda = 0.9$. The projected designs were analyzed using 35 cores of Intel Xeon(R) CPU E5-2680 v4 with 2.40 GHz, and the results are reported in Table 5. The computational and communication time for each analysis was 25 minutes. Table 5 shows that the volume fraction of each case was close to the designed volume fraction, i.e., 35%. However, the projected compliance varied for different periodicity parameters. Obviously, a smaller Λ results in the compliance of the projected design being closer to the homogenized design.

References

[1] A. Tovar, G.L. Niebur, M. Sen, J.E. Renaud, B. Sanders, Bone structure adaptation as a cellular automaton optimization process, in: Proc. of the 45th AIAA/ASME/ASCE/AHS/ASC Structures, Structural Dynamics and Materials Conference, AIAA, Reston, VA, 2004.
[2] L. Dong, Mechanical responses of Ti-6Al-4V truss lattices having a combined simple-cubic and body-centered-cubic (SC-BCC) topology, Aerosp. Sci. Technol. 116 (2021) 106852, https://doi.org/10.1016/j.ast.2021.106852.
[3] T. Fu, Z. Chen, H. Yu, X. Zhu, Y. Zhao, Sound transmission loss behavior of sandwich panel with different truss cores under external mean airflow, Aerosp. Sci. Technol. 86 (2019) 714–723, https://doi.org/10.1016/j.ast.2019.01.050.
[4] G. Totaro, Z. Gürdal, Optimal design of composite lattice shell structures for aerospace applications, Aerosp. Sci. Technol. 13 (4) (2009) 157–164, https://doi.org/10.1016/j.ast.2008.09.001.
[5] Y. Guo, J. Zhang, L. Chen, B. Du, H. Liu, L. Chen, W. Li, Y. Liu, Deformation behaviors and energy absorption of auxetic lattice cylindrical structures under axial crushing load, Aerosp. Sci. Technol. 98 (2020) 105662, https://doi.org/10.1016/j.ast.2019.105662.
[6] M.P. Bendsoe, N. Kikuchi, Generating optimal topologies in structural design using a homogenization method, 1988.
[7] M.P. Bendsoe, O. Sigmund, Topology Optimization: Theory, Methods, and Applications, Springer Science & Business Media, 2013.
[8] E. Sanders, A. Pereira, G. Paulino, Optimal and continuous multilattice embedding, Sci. Adv. 7 (16) (2021) eabf4838.
[9] L. Xia, P. Breitkopf, Multiscale structural topology optimization with an approximate constitutive model for local material microstructure, Comput. Methods Appl. Mech. Eng. 286 (2015) 147–167.
[10] C. Imediegwu, R. Murphy, R. Hewson, M. Santer, Multiscale structural optimization towards three-dimensional printable structures, Struct. Multidiscip. Optim. 60 (2) (2019) 513–525.
[11] J.P. Groen, F.C. Stutz, N. Aage, J.A. Bærentzen, O. Sigmund, De-homogenization of optimal multi-scale 3D topologies, Comput. Methods Appl. Mech. Eng. 364 (2020) 112979.
[12] J. Wu, O. Sigmund, J.P. Groen, Topology optimization of multi-scale structures: a review, Struct. Multidiscip. Optim. 63 (3) (2021) 1455–1480, https://doi.org/10.1007/s00158-021-02881-8.
[13] N. Aage, E. Andreassen, B.S. Lazarov, O. Sigmund, Giga-voxel computational morphogenesis for structural design, Nature 550 (7674) (2017) 84–86.

[14] G. Costa, M. Montemurro, J. Pailhès, A 2D topology optimisation algorithm in NURBS framework with geometric constraints, Int. J. Mech. Mater. Des. 14 (4) (2018) 669–696.
[15] G. Costa, M. Montemurro, J. Pailhès, NURBS hyper-surfaces for 3D topology optimization problems, Mech. Adv. Mat. Struct. 28 (7) (2021) 665–684.
[16] G. Costa, M. Montemurro, J. Pailhès, Minimum length scale control in a NURBS-based SIMP method, Comput. Methods Appl. Mech. Eng. 354 (2019) 963–989.
[17] G. Costa, M. Montemurro, J. Pailhès, N. Perry, Maximum length scale requirement in a topology optimisation method based on NURBS hyper-surfaces, CIRP Ann. 68 (1) (2019) 153–156.
[18] T. Rodriguez, M. Montemurro, P. Le Texier, J. Pailhès, Structural displacement requirement in a topology optimization algorithm based on isogeometric entities, J. Optim. Theory Appl. 184 (1) (2020) 250–276.
[19] G. Costa, M. Montemurro, Eigen-frequencies and harmonic responses in topology optimisation: a CAD-compatible algorithm, Eng. Struct. 214 (2020) 110602.
[20] T. Roiné, M. Montemurro, J. Pailhès, Stress-based topology optimization through non-uniform rational basis spline hyper-surfaces, Mech. Adv. Mat. Struct. (2021) 1–29.
[21] M. Montemurro, G. Bertolino, T. Roiné, A general multi-scale topology optimisation method for lightweight lattice structures obtained through additive manufacturing technology, Compos. Struct. 258 (2021) 113360.
[22] O. Pantz, K. Trabelsi, A post-treatment of the homogenization method for shape optimization, SIAM J. Control Optim. 47 (3) (2008) 1380–1398.
[23] J.P. Groen, O. Sigmund, Homogenization-based topology optimization for high-resolution manufacturable micro-structures, Int. J. Numer. Methods Eng. (2017).
[24] G. Allaire, P. Geoffroy-Donders, O. Pantz, Topology optimization of modulated and oriented periodic microstructures by the homogenization method, Comput. Math. Appl. 78 (7) (2019) 2197–2229.
[25] P. Geoffroy-Donders, G. Allaire, O. Pantz, 3-d topology optimization of modulated and oriented periodic microstructures by the homogenization method, J. Comput. Phys. 401 (2020) 108994, https://doi.org/10.1016/j.jcp.2019.108994.
[26] S. Mukherjee, D. Lu, B. Raghavan, P. Breitkopf, S. Dutta, M. Xiao, W. Zhang, Accelerating large-scale topology optimization: state-of-the-art and challenges, Arch. Comput. Methods Eng. (2021) 1–23.
[27] T.S. Kim, J.E. Kim, Y.Y. Kim, Parallelized structural topology optimization for eigenvalue problems, Int. J. Solids Struct. 41 (9–10) (2004) 2623–2641.
[28] T. Borrvall, J. Petersson, Large-scale topology optimization in 3D using parallel computing, Comput. Methods Appl. Mech. Eng. 190 (46–47) (2001) 6201–6229.
[29] K. Vemaganti, W.E. Lawrence, Parallel methods for optimality criteria-based topology optimization, Comput. Methods Appl. Mech. Eng. 194 (34–35) (2005) 3637–3667.
[30] A. Mahdavi, R. Balaji, M. Frecker, E.M. Mockensturm, Topology optimization of 2D continua for minimum compliance using parallel computing, Struct. Multidiscip. Optim. 32 (2) (2006) 121–132.
[31] N. Aage, B.S. Lazarov, Parallel framework for topology optimization using the method of moving asymptotes, Struct. Multidiscip. Optim. 47 (4) (2013) 493–505.
[32] A. Evgrafov, C.J. Rupp, K. Maute, M.L. Dunn, Large-scale parallel topology optimization using a dual-primal substructuring solver, Struct. Multidiscip. Optim. 36 (4) (2008) 329–345.
[33] E. Wadbro, M. Berggren, Megapixel topology optimization on a graphics processing unit, SIAM Rev. 51 (4) (2009) 707–721.
[34] S. Schmidt, V. Schulz, A 2589 line topology optimization code written for the graphics card, Comput. Vis. Sci. 14 (6) (2011) 249–256.
[35] V.J. Challis, A.P. Roberts, J.F. Grotowski, High resolution topology optimization using graphics processing units (GPUs), Struct. Multidiscip. Optim. 49 (2) (2014) 315–325.
[36] F. Hecht, New development in FreeFem++, J. Numer. Math. 20 (3–4) (2012) 251–266.
[37] B.S. Lazarov, O. Sigmund, Filters in topology optimization based on Helmholtz-type differential equations, Int. J. Numer. Methods Eng. 86 (6) (2011) 765–781.
[38] K. Svanberg, MMA and GCMMA-two methods for nonlinear optimization, vol. 1, 2007, pp. 1–15.
[39] N. Aage, E. Andreassen, B.S. Lazarov, Topology optimization using PETSc: an easy-to-use, fully parallel, open source topology optimization framework, Struct. Multidiscip. Optim. 51 (3) (2015) 565–572.
[40] Y. Tang, A. Kurtz, Y.F. Zhao, Bidirectional Evolutionary Structural Optimization (BESO) based design method for lattice structure to be fabricated by additive manufacturing, Comput. Aided Des. 69 (2015) 91–101.
[41] A.Y. Tamijani, S.P. Velasco, L. Alacoque, Topological and morphological design of additively-manufacturable spatially-varying periodic cellular solids, Mater. Des. (2020) 109155.
[42] K. Gharibi, A.Y. Tamijani, Load-path-based topology optimization of two-dimensional continuum structures, AIAA J. (2021) 1–10.
[43] M. Maldovan, E.L. Thomas, Periodic Materials and Interference Lithography: For Photonics, Phononics and Mechanics, John Wiley & Sons, 2009.
[44] J. Wu, W. Wang, X. Gao, Design and optimization of conforming lattice structures, IEEE Trans. Vis. Comput. Graph. 27 (1) (2019) 43–56.
[45] R.C. Rumpf, J. Pazos, Synthesis of spatially variant lattices, Opt. Express 20 (14) (2012) 15263–15274.
[46] G. Allaire, Shape Optimization by the Homogenization Method, Springer Science & Business Media, 2012.
[47] S. Abhyankar, J. Brown, E.M. Constantinescu, D. Ghosh, B.F. Smith, H. Zhang, PETSc/TS: a modern scalable ODE/DAE solver library, arXiv preprint, arXiv:1806.01437, 2018.
[48] G. Karypis, V. Kumar, A fast and high quality multilevel scheme for partitioning irregular graphs, SIAM J. Sci. Comput. 20 (1) (1998) 359–392.
[49] M.F. Adams, H.H. Bayraktar, T.M. Keaveny, P. Papadopoulos, Ultrascalable implicit finite element analyses in solid mechanics with over a half a billion degrees of freedom, in: SC'04: Proceedings of the 2004 ACM/IEEE Conference on Supercomputing, IEEE, 2004, p. 34.
[50] J. Ahrens, B. Geveci, C. Law, Paraview: an end-user tool for large data visualization, in: The Visualization Handbook, vol. 717, 2005, No. 8.
[51] P. Geoffroy-Donders, Homogenization method for topology optimization of structures built with lattice materials, 2018.
[52] F.C. Stutz, J.P. Groen, O. Sigmund, J.A. Bærentzen, Singularity aware de-homogenization for high-resolution topology optimized structures, Struct. Multidiscip. Optim. 62 (5) (2020) 2279–2295, https://doi.org/10.1007/s00158-020-02681-6.
[53] P. Cignoni, M. Callieri, M. Corsini, M. Dellepiane, F. Ganovelli, G. Ranzuglia, Meshlab: an open-source mesh processing tool, in: Eurographics Italian Chapter Conference, Salerno, Italy, vol. 2008, 2008, pp. 129–136.
[54] D. Locatelli, S.B. Mulani, R.K. Kapania, Wing-box weight optimization using curvilinear spars and ribs (SpaRibs), J. Aircr. 48 (5) (2011) 1671–1684.
[55] D. Locatelli, S.B. Mulani, Q. Liu, A.Y. Tamijani, R.K. Kapania, Supersonic Wing Optimization Using SpaRibs, NASA CR-2014-218537, 2014.
[56] B.K. Stanford, C.V. Jutte, Comparison of curvilinear stiffeners and tow steered composites for aeroelastic tailoring of aircraft wings, Comput. Struct. 183 (2017) 48–60.
[57] M.P. Scardaoni, M. Montemurro, E. Panettieri, PrandtlPlane wing-box least-weight design: a multi-scale optimisation approach, Aerosp. Sci. Technol. 106 (2020) 106156.
[58] X. Lu, Y. Lee, S. Yang, Y. Hao, J.R. Evans, C.G. Parini, Solvent-based paste extrusion solid freeforming, J. Eur. Ceram. Soc. 30 (1) (2010) 1–10.
[59] A.Y. Hussein, The Development of Lightweight Cellular Structures for Metal Additive Manufacturing, 2013.